Motor-Brake-Blending based Roll Stability Enhancement for On Board Motor Electric Vehicles with Torque Vectoring Control

Hiromitsu TOYOTA [1) 2)] Binh-Minh NGUYEN [1)] Sakahisa NAGAI [1)]

Hiroshi FUJIMOTO [1)] Kaoru SAWASE [2)]

1） The University of Tokyo, Kashiwa, Chiba, Japan

2）Mitsubishi Motors Corporation, Okazaki, Aichi, Japan

E-mail: hiromitsu.toyota@mitsubishi-motors.com

ABSTRACT: The importance of 6 Degree-of-Freedom (DOF) motion control using electric motors has increased with the shift from Internal Combustion Engine (ICE) Vehicle to Electric Vehicle (EV). There are two types of EV motors, one is In-Wheel-Motors (IWM) and the another is On-Board-Motor (OBM). Although OBM has been the mainstream for mass-produced vehicles, OBM-EV has a lower sprung posture control performance compared to IWM-EV. To overcome this issue, it is possible to integrate OBM with the Friction Brake Systems (FBS) that have the same sprung posture control effect as IWM. However, FBS has lower response speed than that of OBM. This study proposes an OBM-FBS collaboration control method to increase the sprung posture stabilization during torque vectoring, thereby further resolving the phase shift issue between OBM and FBS. After presenting the theoretical framework of the proposed method, its control effectiveness is validated through real vehicle experiments.

KEY WORDS: Vehicle Dynamics, Motion control, On Boad Motor, Friction Brake System, Torque Blending, Frequency Separation.

1. INTRODUCTION

The importance of vehicle handling and roll stability through driving force control has been increasingly recognized [(1)(2)]. As key control technologies to address this issue, there are already methods for enhancing planar 3DOF motion using electric motors or FBS separately, such as Torque Vectoring Control (TVC) [(3)(4)(5)(6)], as well as technologies for controlling the sprung mass posture [(7)(8)]. Furthermore, there are cooperative control technologies between electric motors and FBS to enhance the planar 3DOF motion performance [(9)(10)] and stabilize the roll dynamics [(11)(12)].

However, almost all of the aforementioned studies focused on IWM instead of the mainstream On-Board-Motor-System (OBMS) found in current production vehicles. There exists prior work on improving planar 3DOF dynamics and stabilizing roll behavior using OBMS and FBS [(13)]. However, the technology [(13)] merely switches actuator controls according to priority, operates around the maximum tire friction performance, and does not actively coordinate driving force and braking force from areas with low lateral acceleration. In addition, as controlling FBS with a fast response speed generates unpleasant noises, its control performance in the normal range is limited. Furthermore, these prior studies did not address the difference in response characteristics between OBMS and FBS. This raises concerns about control instability caused by phase differences in actuator operation when tightly coordinating OBMS and FBS.

With respect to the above issues, based on a vehicle prototype with torque vectoring function, this paper establishes a methodology that properly addresses the response difference between OBMS and FBS, and proposes a control law that achieves both improvement of planar 3DOF dynamics and stabilization of roll behavior.

The contribution of this study is threefold:

First, a frequency separation method is proposed to stabilize the OBMS-FBS collaborative system during TVC.

Second, we theoretically showed that the stability of the proposed system is improved compared with the conventional collaboration methods.

Last but not least, the effectiveness of the proposed method was successfully verified using real vehicle tests.

The remainder of this article is structured as follows: Section 2 clarifies the impact of TVC on roll dynamics and the problem of wheel torque control allocation. Section 3 proposes the roll dynamics stabilization method during TVC using frequency separation control. Section 4 theoretically analyzes and compares system stability using the conventional method and the proposed method. Real vehicle evaluation results are discussed in Section 5. Finally, the conclusion is stated in Section 6.

2. SPRUNG POSTURE DYNAMICS BY TVC

2.1. Driving and Braking force effect on vertical forces

Currently, there are several different types of suspension. They are generally summarized as in Table 1[14].

Table 1 Summary of Suspension Type

		Suspension Type	
		Front Suspension	Rear Suspension
Vehicle Category	Small size	Strut	(2WD) Torsion Beam (4WD) De Dion etc.
	Mid size		
	Big size		Double Wishbone Multi Link
	High Perf.	Double Wishbone Multi Link	
	Frame		Rigid Axle

Since the suspension must be designed based on various constraints such as ride comfort and handling stability, it is impossible to design the suspension type or the geometry by considering only the sprung behavior. Furthermore, the suspension geometry must be designed within limited conditions according to the suspension type. In case of combinations, the effect of the driving and braking forces on the sprung posture would be bigger by the rear than by the front.

2.2. Effect on sprung posture dynamics

The driving force of the OBMS is not transferred to the suspension but to the vehicle body via the differential gear. Therefore, the driving force of each wheel effects as a vertical force divided by the tangent of the angle (θ_{anu}^{OBM}, θ_{asq}^{OBM}) between the tire wheel center and the suspension Instantaneous Center of Rotation (ICR). On the other hand, the FBS force is transferred to the vehicle body via the suspension mechanism. Consequently, the braking force of each wheel effects as a vertical force divided by the tangent of the angle (θ_{and}^{FB}, θ_{atl}^{FB}) between the tire contact point of road and the suspension ICR. In addition, since IWM also influenced the vehicle body via suspension, IWM has the same effect to the vertical force as FBS. As shown in Fig. 1, $\theta_{anu(asq)}^{OBM}$ is usually smaller than $\theta_{and(atl)}^{FB}$. Thus, the vertical force caused by OBMs are smaller than those generated by IWMs and FBSs.

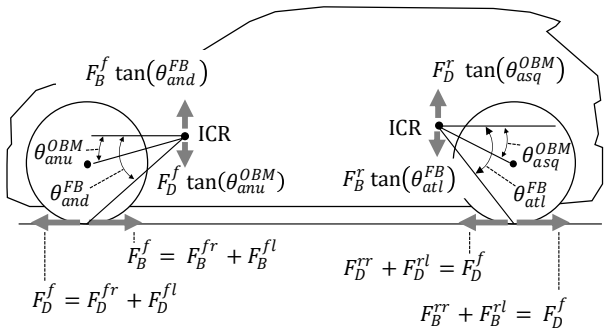

Fig. 1 Anti-Tail Lift Force, Anti-Squat Force, Anti-Nose−Dive Force, Anti-Nose-Up Force

The relationships between vertical and longitudinal forces are shown in Fig.1 where F_D^i, F_B^i are the braking and driving forces of each wheel ($i = fr, fl, rr, rl$).

2.3. Driving and Braking force effect on roll moment

The left-hand side of Fig. 2 shows the optimal driving force distribution during right turning. As shown in this figure, the vertical load on the left wheel becomes larger than the right wheel, therefore it can increase the driving force of the outer wheel and need to decrease the driving force on the inner wheel according to this vertical load, the tire's performance can be maximized. In addition, by controlling the Direct Yaw Moment (DYM) M_z^{DYM} generated via braking and driving force differences between the left and right wheels, it is possible to further improve handling stability and the planar 3DOF performance [14].

From the point of view of roll motion, if the actual yaw rate is smaller than the target yaw rate during TVC, the rear axle Direct-Roll-Moment (DRM) M_x^{DRM} effects in the opposite direction to the roll moment by the centrifugal force M_x^G, thereby reducing the roll angle as shown in Fig. 2. On the other hand, since the front axle DRM effects in the same direction as the roll moment M_x^G by centrifugal force, it effects to increase the roll moment as shown in Fig. 2.

With respect to the discussion in the previous sub-section, the additional DRM generated during the TVC are expressed as in equations (2.1) and (2.2). As can be understood from these formulas, if the actual yaw rate is lower than the target yaw rate during TVC, TVC using rear driving and braking forces can stabilize the sprung posture dynamics more than TVC using front driving and braking forces.

Transparently, to achieve stabilization of the roll posture with increase yaw rate and lateral acceleration by TVC, it is necessary to operate TVC at the rear axle.

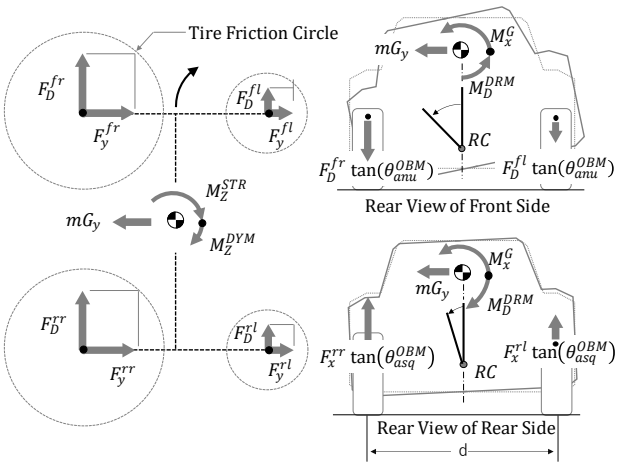

Fig. 2 Force Distribution and Direct Roll Moment

$$M_x = M_x^G + M_x^{DRM} \tag{2.1}$$

$$\begin{aligned} M_x^{DRM} = &\frac{d}{2}\tan(\theta_{anu}^{OBM})\,[-1 \quad 1]\begin{bmatrix}F_D^{fl}\\F_D^{fr}\end{bmatrix} \\ &+\frac{d}{2}\tan(\theta_{asq}^{OBM})\,[1 \quad -1]\begin{bmatrix}F_D^{rl}\\F_D^{rr}\end{bmatrix} \\ &+\frac{d}{2}\tan(\theta_{and}^{FB})\,[1 \quad -1]\begin{bmatrix}F_B^{fl}\\F_B^{fr}\end{bmatrix} \\ &+\frac{d}{2}\tan(\theta_{atl}^{FB})\,[-1 \quad 1]\begin{bmatrix}F_B^{rl}\\F_B^{rr}\end{bmatrix} \end{aligned} \tag{2.2}$$

3. PROPOSAL CONTROL METHOD

3.1. Vehicle Modeling

Fig.3 shows the vehicle's planar 3DOF model. The variables and parameters in Fig.3 are defined as follows. Vehicle velocity is denoted by V, steering angle is δ_f, yaw rate is γ, DYM is M_z^{DYM}. The distances between the vehicle's COG and the front and rear axle are l_f and l_r, while the trackwidth is represented by d. The longitudinal and lateral velocities are v_x, v_y. The vehicle body and front and rear tire slip angles are β, β_f, β_r, The longitudinal driving and braking forces on each wheel F_D^i, F_B^i. Let M_z^{DYM} and δ_f be the inputs and let γ and β be the outputs, the vehicle planar dynamics are expressed as in (3.1) and (3.2) [14][15].

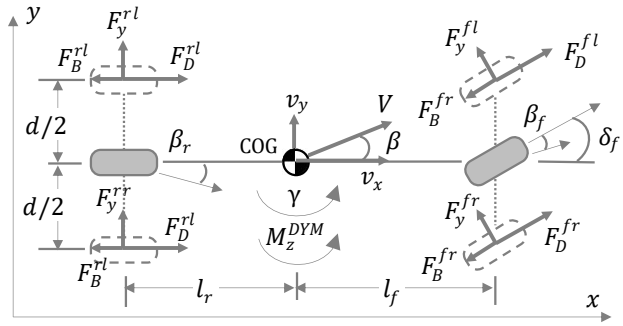

Fig. 3 Vehicle Planar Dynamics

$$\begin{bmatrix}\beta\\ \gamma\end{bmatrix} = \begin{bmatrix}P_{\delta_f\to\beta}(s) & P_{M_z\to\beta}(s)\\ P_{\delta_f\to\gamma}(s) & P_{M_z\to\gamma}(s)\end{bmatrix}\begin{bmatrix}\delta_f\\ M_z^{DYM}\end{bmatrix} \tag{3.1}$$

where $P_{\delta_f\to\beta}(s)$, $P_{\delta_f\to\gamma}(s)$, $P_{M_z\to\beta}(s)$, $P_{M_z\to\gamma}(s)$ and $\vartheta_\gamma(s)$ are as follows:

$$\begin{bmatrix}P_{\delta_f\to\beta}(s) & P_{M_z\to\beta}(s)\\ P_{\delta_f\to\gamma}(s) & P_{M_z\to\gamma}(s)\end{bmatrix} = \vartheta_\gamma(s)\begin{bmatrix}s-a_{22} & a_{12}\\ a_{21} & s-a_{11}\end{bmatrix}\begin{bmatrix}b_{11} & b_{12}\\ b_{21} & b_{22}\end{bmatrix} \tag{3.2}$$

$$\vartheta_\gamma(s) = \frac{1}{s^2-(a_{12}+a_{21})s + a_{11}a_{22} - a_{12}a_{21}}$$

where $a_{11} \sim b_{22}$ are defined as follows

$$\begin{aligned} a_{11} &= -\frac{2(C_f+C_r)}{mv_x} \quad , \quad a_{12} = -1 - \frac{2(C_f l_f - C_r l_r)}{mv_x} \\ a_{21} &= -\frac{2(C_f l_f - C_r l_r)}{I_z} \quad , \quad a_{22} = -\frac{2(C_f l_f^2 - C_f l_f^2)}{I_z v_x} \\ b_{11} &= \frac{2C_f}{mv_x} \quad , \quad b_{12} = 0 \quad , \quad b_{21} = \frac{2C_f l_f}{I_z}, \quad b_{22} = \frac{1}{I_z} \end{aligned}$$

where I_z is the yaw moment of inertia. Besides, the role dynamics model of the vehicle is given by the following equations (3.3) and (3.4):

$$\phi = V_r(s)[mh \quad 1]\begin{bmatrix}G_y\\ M_x^{DRM}\end{bmatrix} \tag{3.3}$$

$$V_r(s) = \frac{1}{I_x s^2 + C_x s + (K_x - mh)} \tag{3.4}$$

The parameters in (3.3) and (3.4) are defined as follows. I_x is the roll moment of inertia. C_x and K_x are the damping coefficient and spring stiffness coefficient including the suspension, stabilizer, and tire characteristics, respectively. ϕ is the roll angle, r is the tire radius, s is the Laplace operator, m is the vehicle mass, h is the distance between the line connecting the rear and front roll centers (RC) and the COG. G_y is the lateral acceleration.

3.2. System Block Diagram

Fig. 4 shows the block diagram of the proposed control system where the integrated plant of the planar 3DOF dynamics and roll dynamics are established using (3.1) ~ (3.4).

Assuming that the FBS and OBMS at each wheel can be controlled independently, the torque blending block and drive & brake actuation block can be expressed using $\{D, Q(s), H(s), N, R\}$, as can be shown in (3.5) ~ (3.10).

In Fig. 4, M_z^* and γ^* are the yaw moment and reference yaw rate. Vector T^* includes the target braking and driving torques, while vector T includes the actual braking and driving torques.

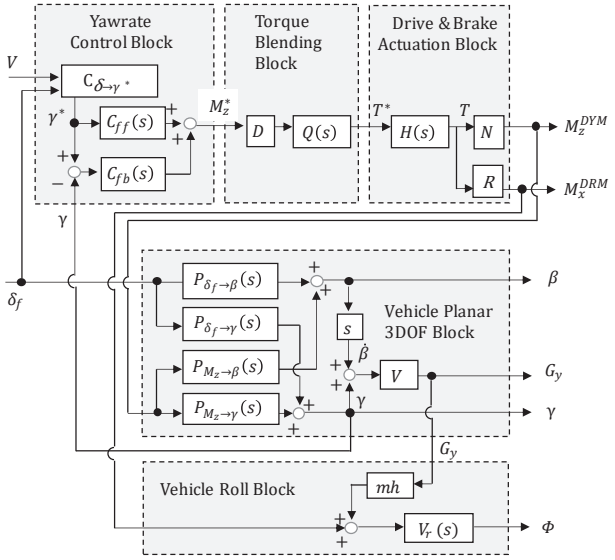

Fig.4 Proposed System with Vehicle Plant Diagram

$$D = \frac{d}{r}[-1 \quad 1 \quad -1 \quad 1 \quad -1 \quad 1 \quad -1 \quad 1]^T \tag{3.5}$$

$$Q(s) = \mathrm{diag}[Q_m^{fl}(s) \quad Q_m^{fr}(s) \quad Q_m^{rl}(s) \quad Q_m^{rr}(s) \quad Q_b^{fl}(s) \quad Q_b^{fr}(s) \quad Q_b^{rl}(s) \quad Q_b^{rr}(s)] \tag{3.6}$$

$$H(s) = \mathrm{diag}[H_m^{fl}(s) \quad H_m^{fr}(s) \quad H_m^{rl}(s) \quad H_m^{rr}(s) \quad H_b^{fl}(s) \quad H_b^{fr}(s) \quad H_b^{rl}(s) \quad H_b^{rr}(s)] \tag{3.7}$$

$$N = \frac{d}{r}[-1 \quad 1 \quad -1 \quad 1 \quad -1 \quad 1 \quad -1 \quad 1] \tag{3.8}$$

$$R = \frac{d}{r}[-D_f \quad D_f \quad -D_r \quad D_r \quad -B_f \quad B_f \quad -B_r \quad B_r] \tag{3.9}$$

$$D_f = tan(\theta_{anu}^{OBM}), D_r = tan(\theta_{asq}^{OBM})$$
$$B_f = tan(\theta_{and}^{FB}), B_r = tan(\theta_{atl}^{FB}) \tag{3.10}$$

As mentioned in Section 2 to achieve stabilization of the roll posture with increase yaw rate and lateral acceleration by TVC, it is necessary to operate TVC at the rear axle. When TVC is performed by the rear axle, it is possible to utilize the IWM system shown in Fig. 5 that can drive the left and right wheels independently. In addition, the anti-nosedive angle and anti-tail lift angle of the IWM are the same as those of the FBS, so they are larger than those of the OBM and are therefore more effective in controlling the sprung posture motion.

While the IWM can directly drive the torque of each wheel, the posture control and the driving torque of each wheel depends on the motor capability. Also, the torque difference between the left and right wheels is limited by the motor output. Thus, the yaw moment cannot be generated beyond the motor performance limitation. In addition, since the left and right wheels are not mechanically connected, it is not possible to improve traction performance on slippery roads by directly connecting the two wheels like a mechanical differential lock mechanism. Therefore, a torque difference amplification type TDA-TVD (Torque Difference Amplification Torque Vectoring Differential) with a two-input, two-output mechanism shown in Fig. 6. This system has been proposed to amplify the torque difference between the left and right motors and output a yaw moment greater than the motor output [16][17]. This TDA-TVD is the same as IWM system in that it drives the left and right wheels with two OBM and is characterized by the presence of a mechanical coupling between the left and right wheels by planetary gears. Compared to the IWD-TVD, which uses the same performance motor, the TDA-TVD amplifies the torque difference between the left and right wheels and can generate a larger direct yaw moment._TDA-TVD can be designed bigger value of K_T in (3.12) than 1.

In addition, on slippery roads where one wheel cannot generate drive torque, the IWM-TVD can only generate drive torque from the motor on the opposite side, but the TDA-TVD can increase K_T time the drive torque of the opposite wheel e.g. $T_d^{TDA} = K_T T_m^{rr}$. From the perspective of TVC, the TDA-TVC is thus an extremely excellent OBMS. Therefore, this paper uses the OBM of TDA-TVD for verification. The brake system use electric calipers that can be controlled independently on each of the four wheels.

$$\Delta T_d^{IWM} = T_m^{rr} - T_m^{rl} \tag{3.11}$$

$$\Delta T_d^{TDA} = K_T(T_m^{rr} - T_m^{rl}) \tag{3.12}$$

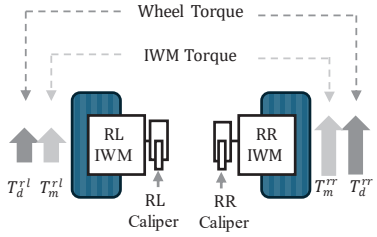

Fig. 5 Schematic diagram of IWM

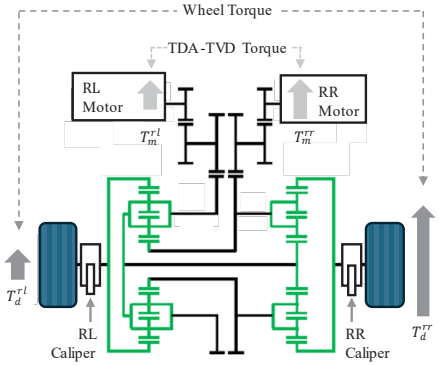

Fig. 6 Schematic diagram of TDA-TVD.

Considering the TDA-TVD system of OBMS and electric calipers of FBS using rear axle, there are 4 actuators represented by $H(s)$. Thus, the torque blending and actuators models are formulated as follows:

$$D = \frac{d}{r}[-1 \quad 1 \quad -1 \quad 1]^T \tag{3.13}$$

$$Q(s) = \mathrm{diag}[Q_m^{rr}(s) \quad Q_m^{rr}(s) \quad Q_b^{rl}(s) \quad Q_b^{rr}(s)] \tag{3.14}$$

$$H(s) = \mathrm{diag}[H_m^{rl}(s) \quad H_m^{rr}(s) \quad H_b^{rl}(s) \quad H_b^{rr}(s)] \tag{3.15}$$

$$N = \frac{d}{r}[-1 \quad 1 \quad -1 \quad 1] \tag{3.16}$$

$$R = \frac{d}{r}[-D_r \quad D_r \quad -B_r \quad B_r] \tag{3.17}$$

The vertical force generated by the FBS is greater than that generated by the OBMS, so the use of the FBS can stabilize the roll behavior. However, to perform active pressure control and differential pressure control within a range where the driver and passengers do not perceive the FBS operation sound as noise, there is a restriction that it can only be operated in the low frequency range. On the other hand, the OBMS has a fast response and can perform control in the high frequency range. Here, the FBS transfer functions $H_b^{rl,rr}(s), H_m^{rl,rr}(s)$ are shown as (3.18), (3.19). Note that frequency analysis is only required in a range that can cover the responsiveness of yaw rate and roll. Thus, the system modelling can consider the range up to about 10[Hz]. Consequently, higher-order models above 10[Hz] can be omitted, and we can treat (3.18) and (3.19) as 2nd order transfer functions. In addition, $H_b^{rl,rr}(s)$ incorporates a low-pass filter to prevent the FBS operation sound from being recognized as noise, in addition to the actual FBS responsiveness.

$$H_b^{rl,rr}(s) = \frac{{\omega_b^{rl,rr}}^2}{s^2 + 2\,\zeta_b^{rl,rr}\,\omega_b^{rl,rr}\,s + {\omega_b^{rl,rr}}^2} \tag{3.18}$$

$$H_m^{rl,rr}(s) = \frac{{\omega_d^{rl,rr}}^2}{s^2 + 2\,\zeta_d^{rl,rr}\,\omega_d^{rl,rr}\,s + {\omega_d^{rl,rr}}^2} \tag{3.19}$$

$$Q_b^{rl,rr}(s) = k \times \left(\frac{\omega_b^{rl,rr}}{s + \omega_b^{rl,rr}}\right) \tag{3.20}$$

$$Q_m^{rl,rr}(s) = 1 - k \times Q_b^{rl,rr}(s) \tag{3.21}$$

$$0 \leqq k \leqq 1 \tag{3.22}$$

The frequency separation control design method is to design a filter so that the cutoff frequency of $Q_b^{rl,rr}(s)$ does not exceed the cutoff frequency of $Q_m^{rl,rr}(s)$. The function $Q_m^{rl,rr}(s)$ is design to be $Q_m^{rl,rr}(s) = 1 - k \times Q_b^{rl,rr}(s)$ (High pass filter) because OBMS response $H_m^{rl,rr}(s)$ is higher than the FBS response $H_b^{rl,rr}(s)$. The value k is the design coefficient of FBS and OBMS. If it is needed to stabilize the roll dynamics, it needs to increase the k value. If it is required to reduce brake pad wear and energy loss, it needs to decrease the k value. Thus, k is a value that is determined according to the target vehicle performance. Here, the cutoff frequency $\omega_b^{rl,rr}$ of formula $H_b^{rl,rr}(s)$ is used as the cutoff frequency of formula $Q_b^{rl,rr}(s)$. This is to design the gain of formula $Q_b^{rl,rr}(s)$ so that it does not exceed the gain of formula $H_b^{rl,rr}(s)$ at low frequencies. In addition, the frequency separation filter $Q_b^{rl,rr}(s), Q_m^{rl,rr}(s)$ of the proposed method is configured to be incorporated between the target yaw rate γ^* and the FBS plant $H_b^{rl,rr}(s)$ and the OBMS plant $H_m^{rl,rr}(s)$, and the control signal T^* is shown in (3.23).

$C_{ff}(s)$ is the inverse model of $P_{Mz\to\gamma}(s), C_{fb}(s)$ uses PID control, and $C_{\delta\to\gamma^*}$ is as shown in formula (3.24). In this formula, V is the vehicle speed, A is the stability factor, and L is the wheelbase. K_f and K_r are tire cornering stiffness.

$$T^* = Q(s)D\left[\left(C_{ff}(s) + C_{fb}(s)\right)C_{\delta\to\gamma^*} \quad -C_{fb}(s)\right]\begin{bmatrix}\delta_f \\ \gamma\end{bmatrix} \tag{3.23}$$

$$C_{\delta\to\gamma^*} = \frac{1}{1 + AV^2}\frac{V}{L} \quad A = -\frac{m}{2L^2}\frac{l_f K_f - l_r K_r}{K_f K_r} \tag{3.24}$$

4. SYSTEM STABILITY ANALYSIS

4.1. Problem setting

The filter $Q_m^{rl,rr}(s), Q_b^{rl,rr}(s)$ of the proposed method is a part of the yaw rate feedback system. Therefore, system stability analysis is needed to evaluate different selections of the OBM and FBS integration. The control stability analysis is confirmed using a Nyquist diagram. In this paper, as shown in Table 2, the method without FBS is defined as the conventional method 1[CM1], the control method that does not consider the frequency characteristics of FBS and OBMS is defined as the conventional method 2[CM2], and the control method that considers the frequency characteristics of FBS and OBMS is defined as the proposed method [PM].

The block diagram of the open loop transfer function $L(s)$ is shown in Fig. 7, and the formula is as shown in formulas (4.1). In this formulas, $Q_m^{rl,rr}(s), Q_b^{rl,rr}(s)$ are as Tabel 2.

Table 2 Control Method

No.	Control Method	$Q_m^{rl,rr}(s), Q_b^{rl,rr}(s)$
[CM1]	Only OBMS Conventional Method 1	$Q_m^{rl,rr}(s)$ =1.0 , $Q_b^{rl,rr}(s)$ =0.0 (Fixed Value)
[CM2]	FBS and OBMS Fixed Ratio Conventional Method 2	$Q_m^{rl,rr}(s) = 1 - k$, $Q_b^{rl,rr}(s) = k$ (Fixed Value)
[PM]	FBS and OBMS Frequency Separation Proposing Method	$Q_m^{rl,rr}(s)$ ×(1- k) , $Q_b^{rl,rr} \times k$

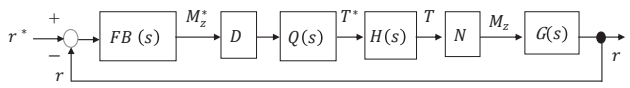

Fig. 7 Equivalent diagram for Stability Analysis

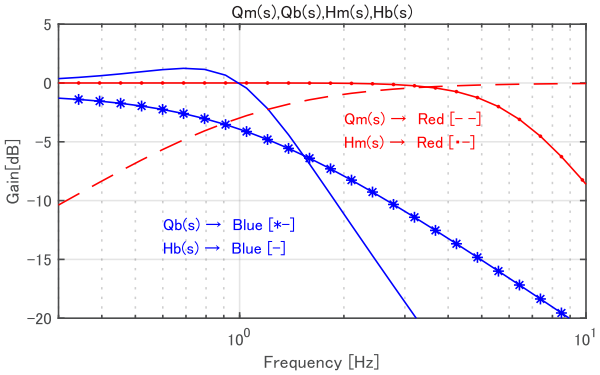

Fig.8 Plant and Frequency Separation Filter

$Q_m^i(s), Q_b^i(s), H_m^i(s), H_b^i(s)$

$$L(s) = G(s) \cdot N \cdot H(s) \cdot Q(s) \cdot D \cdot C_{fb}(s) \qquad (4.1)$$

The vehicle specifications are shown in Table 3. The parameters of the OBMS characteristic $H_m^{rl,rr}(s)$ is acquired by system identification of evaluation vehicle . As a result, the cutoff frequency and damping coefficient of $H_m^{rl,rr}(s)$ were $\omega_d^{rl,rr} = 6.3 \times 2\pi$, $\zeta_d^{rl,rr} = 0.7$. Regarding the FBS, 1 [Hz] low-pass filter was placed after $Q_b^{rl,rr}(s)$ to consider the operating noise, and the characteristics of $H_b^{rl,rr}(s)$ include this low-pass filter. As a result of combining the FBS responsiveness and the 1 [Hz] low-pass filter, the cutoff frequency and damping coefficient of $H_b^{rl,rr}(s)$ are $\omega_d^{rl,rr} = 2\pi$, $\zeta_b^{rl,rr} = 1.0$. The k value of the frequency separation filter is set to 0.9 to stabilize the sprung behavior.

Table 3 Vehicle Specs

Contents	Symbol	Value	Unit
Vehicle Wight	m	2200	[kg]
Vehicle Height	h	0.635	[m]
Cornering Stiffness	C_f, C_r	110, 85.5	[kN/rad]
COG. to Axle Length	l_f, l_r	1.39, 1.28	[m]
Wheelbase	L	2.67	[m]
Anti-Force Angle	θ_{asq}^{OBM}, θ_{atl}^{FB}	7.2 , 22.9	[deg]
Roll Inertia	I_x	712.3	[kgm2]
Roll Dumping	C_x	9538.5	[Nm/(rad/s)]
Roll Stiffness	K_x	63368	[Nm/rad]

4.2. Stability analysis using Nyquist diagrams

The Nyquist stability analysis results of the open loop transfer function $L(s)$ are shown in Fig 9.

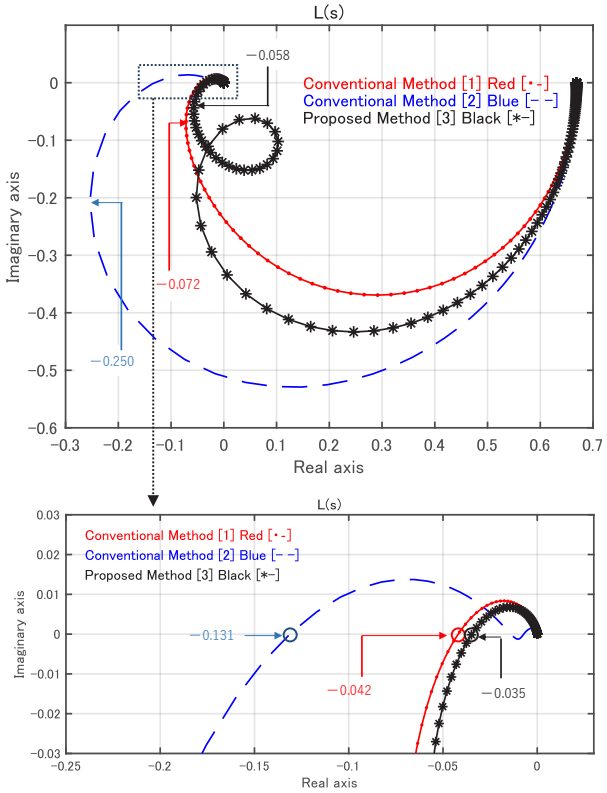

Fig.9 Nyquist Diagram

The results of the Nyquist stability analysis using the open loop transfer function $L(s)$ for the control methods [CM1], [CM2] and [PM] in Table 2 are shown in Fig. 9. As shown in the upper part of Fig. 9, the values of the smallest value on the real axis are respectively -0.072, -0.250, and -0.058, which are sufficient margins. Therefore, [CM1], [CM2] and [PM] all stabilize the control systems. The lower part of Fig. 9 is an enlarged view of the area where [CM1], [CM2], and [PM] cross the real axis. The crossing points have the real value of -0.042 for [CM1] and -0.035 for [PM], confirming that stability has improved. Furthermore, although the crossing point of [CM2] has the real value of -0.131, it is closer to point (-1, 0) than [CM1] and [PM]. This indicates that system stability has reduced by [CM2].

5. EVALUATION RESULTS

In this paper, the control laws of [CM1], [CM2], and [PM] are compared and verified on an actual vehicle. To this end, this study uses the evaluation vehicle shown in Fig. 10. This is a plug-in hybrid vehicle with a control brake system, and it can control each wheel braking force independently and torque vectoring device that can transfer torque between the left and right wheels using two motors in the rear. And an engine, generator, and motor in the front. The evaluation condition is described in Table 4.

Fig.10 Experimental Vehicle

This study uses the evaluation vehicle shown in Fig. 10. This vehicle is a plug-in hybrid vehicle with a control brake system, and it can control each wheel braking force independently and torque vectoring device that can transfer torque between the left and right wheels using two motors in the rear. And an engine, generator, and motor in the front. The evaluation maneuver is in Table 4.

Table 4 Test Maneuver and Condition

Contents	Condition
Condition	DRY
Driving Pattern	Steady Circular Turn
Vehicle Speed	47[km/h]
Steering Angle	110 [deg]

Fig. 11 shows the time series data of lateral acceleration G_y, yaw rate, and roll angle. The left column of Fig. 11 shows the conventional method [CM1], the middle column shows the conventional method [CM2], and the right column shows the proposed method [PM]. To measure sufficiently stable data in this evaluation, data was measured for about 2-circle turn (about 26 seconds) after the steady-state turning behavior stabilized.

As for the vehicle planner 3DOF motion performance, all the control methods above show the same performance, as shown by the lateral acceleration G_y and yaw rate. Furthermore, as shown by the rear roll angle, the roll angle of the [PM] is respectively reduced by 11% and 6% in comparison with that of the [CM1] and [CM2].

The reduction in roll angle is noticeable by drivers. In particular, the comfort of the rear seats is significantly improved compared to the driver's seat, making this technology effective for vehicles with three rows of seats or with a high center of gravity.

The evaluation results are summarized in Table 5. Compared to the conventional methods [CM1] and [CM2], the proposed method [PM] achieved significant improvements in roll behavior stabilization without compromising control stability and planar 3DOF steering performance, proving that it can make a significant contribution to reducing roll during torque vectoring.

6. CONCLUSION

In this paper, a frequency separation method was proposed to enhance the roll stability of onboard motor vehicles. The proposed method effectively integrates the motor and braking actuators, which have different respond capabilities. The proposed method was evaluated using real-vehicle experiments. Compared to conventional methods, the proposed method achieved significant improvements in roll behavior stabilization without compromising control stability and planar 3DOF steering performance, proving that it can make a significant contribution to reducing roll during torque vectoring. In future, we will expand the proposal to not only the roll motion but also 6DOF control using OBMS.

Table 5 Evaluation Results

Control Method	Control Stability	Planner Performance	Sprung Performance
[CM1]	Base	Base	Base
[CM2]	Poor [-]-0.070 →-0.168	Same as Base	Improved
[PM]	Improved [+]-0.070 →-0.045	Same as Base	Improved [++] 9%

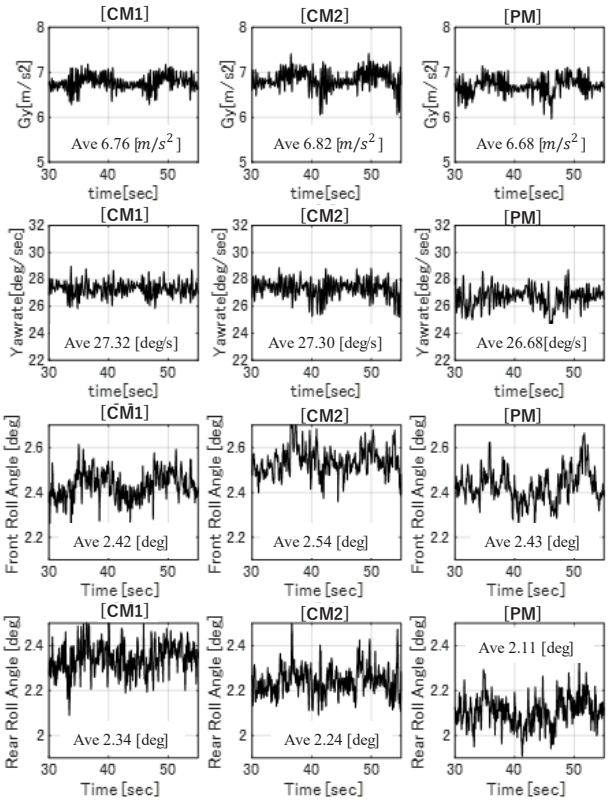

Fig. 11. Evaluation Results of Control Method [CM1][CM2][PM]

References

(1) J. Yoon, W. et al.: “Unified chassis control for rollover prevention and lateral stability,” IEEE Transactions on Vehicular Technology. Vol. 58, No. 2, pp. 596-609 (2009)

(2) R. Rajamani et al.: “New paradigms for the integration of yaw stability and rollover prevention functions in vehicle stability control,” IEEE Transactions on Intelligent Transportation System, Vol. 14, No. 1, pp. 249-261, (2013)

(3) Hiroyuki Fuse, Hiroshi Fujimoto: “Cornering Force Maximization with Variable Slip Ratio Control for Independent All-Wheel-Drive Electric Vehicle, IEEE Journal of Emerging and Selected Topics in Industrial Electronics, Vol. 4, No. 1, pp. 381-388 (2023)

(4) Takumi Ueno, Binh-Minh Nguyen, Hiroshi Fujimoto: “Driving Force Control for In-Wheel Motor Electric Vehicles with Wheel Speed Limiter and Absolute Stability Analysis,” 49th Annual Conference of the IEEE Industrial Electronics Society, pp. 1-6 (2023).

(5) Tona Sato, Takumi Ueno, Binh- Minh Nguyen, Hiroshi Fujimoto, Hiromitsu Toyota and Kaoru Sawase: “Sideslip Angle Based Variable Slip Ratio Limiter for Direct Yaw Moment Control of Two-Input-Two-Output Motor Vehicles,” 2024 IEEE International Conference on Advanced Intelligent Mechatronics (AIM), pp. 1476-1481 (2024)

(6) Zhenpo Wang et al.: “Automotive ABS/DYC Coordinated Control Under Complex Driving Conditions,” IEEE Access, Vol. 6, pp. 32769 – 32779 (2018)

(7) Tomonori Suzuki, Masahiro Mae, Hiroshi Fujimoto, et al.: “Model-based Filter Design for Triple Skyhook Control of In-Wheel Motor Vehicles for Ride Comfort,” IEEJ Journal of Industry Applications, Vol. 10, Iss. 3, pp 310-316 (2021)

(8) Enguo Dong et al.: “Research for Vehicle Anti Rollover Control Based on Differential Braking,” International Conference on Computer Network, Electronic and Automation (ICCNEA China) (2019)

(9) Xie Shaobo et al.: “Stability control of a dual motor vehicle based on coordinated application of motor and hydraulic actuator,” 4th International Conference on Power Electronics Systems and Applications (China), (2011)

(10) Reza Hajiloo et al.: “Integrated Lateral and Roll Stability Control of Multi-Actuated Vehicles Using Prioritization Model Predictive Control,” IEEE Transactions on Vehicular Technology, Vol. 71, Iss. 8, pp 8318 – 8329 (2022)

(11) Etsuo Katsuyama: “Research on integrated control of 6-degree-offreedom vehicle motion in the era of electrified drive systems,” Kanagawa Institute of Technology, Department of Mechanical Systems Engineering, Doctoral thesis (2022)

(12) Sota Ukai et al.: “Integrated control of 6-component vehicle motion using brakes on each wheel,” Transactions of the Society of Automotive Engineers of Japan, Vol. 53, No. 5, p. 942-947 (2022).

(13) Reza Hajiloo et al.: “Integrated Lateral and Roll Stability Control of Multi-Actuated Vehicles Using Prioritization Model Predictive Control,” IEEE Transactions on Vehicular Technology, Vol.71, Iss. 8, pp 8318 – 8329 (2022).

(14) Takaaki Uno: “Vehicle Dynamics and Chassis Mechanisms,” 2nd Edition, Grand Prix Publishing (2021).

(15) Masato Abe: “Vehicle Dynamics and Control,” Tokyo Denki University Press (2008)

(16) Kaoru Sawase, Motoharu Chiba: “Study of Lateral Torque-vectoring Differential Suitable for Electric Powered Vehicles", Transactions of Society of Automotive Engineers of Japan, Vol.45-5, pp. 823-828 (2014) (In Japanese).

(17) Kaoru Sawase et.al.: “Classification and Analysis of Torque-vectoring Differentials with Torque Difference Amplification Mechanism,” Transactions of Society of Automotive Engineers of Japan, Vol.48, No.2, pp.317-322, (2017) (In Japanese).